Role of inversion symmetry and multipole effects in nonresonant x-ray Raman scattering from icosahedral B$_4$C

Yejun Feng,[1] G. T. Seidler,[1,2,*] J. O. Cross,[1,2] A. T. Macrander,[3] and J. J. Rehr[1]

[1]*Department of Physics, University of Washington, Seattle, Washington 98195-1560, USA*
[2]*PNC-CAT, Advanced Photon Source, Argonne National Laboratory, Argonne, Illinois 60439, USA*
[3]*Advanced Photon Source, Argonne National Laboratory, Argonne, Illinois 60439, USA*

We report nonresonant x-ray Raman scattering (XRS) measurements for the icosahedral boron carbide B$_4$C for transferred momentum q from 1 to 9 Å^{-1}. The observed q-dependence together with site-specific *ab initio* calculations identify a near-edge peak in the XRS spectra as a p-type ($\Delta l = 1$) exciton due to dominant boron occupation at the sole atomic site in the unit cell having inversion symmetry. This result constrains models of substitutional disorder in B$_4$C, introduces a new application of XRS, and emphasizes the utility of full multiple scattering calculations of the site-specific projected density of states for interpretation of the near edge region of XRS spectra.

PACS number(s): 61.72.Ss, 61.10.Ht, 71.35.−y

I. INTRODUCTION

Icosahedral boron-rich compounds[1] have enjoyed several decades of intense study[1–12] as a result of their extreme mechanical strength,[2–4] interesting electronic and optical properties,[5] and the frequent occurrence of icosahedral structures.[1] The icosahedral configuration is the result of a tendency for three-centered covalent bonds due to a deficiency of valence electrons.[6–8] Examples of icosahedral phases include all four crystalline phases of boron[9,10] and other boron rich materials such as B$_4$C, B$_{12}$As$_2$, B$_{12}$P$_2$,[1] B$_6$O,[11] and YB$_{66}$.[12]

Among all the icosahedral boron materials, the site-substitutionally disordered boron carbide B$_4$C represents a special interest.[13–34] Strictly speaking, B$_4$C is a class of materials with a stoichiometry of B$_{12+x}$C$_{3-x}$, for which the carbon concentration varies continuously from 9 to 19 at. % ($0.06 < x < 1.7$).[13] Neutron[14] and x-ray[15–19] diffraction studies find a rhombohedral crystal structure (see Fig. 1) with the unit cell consisting of 15 atoms with 12 atoms at icosahedral sites (the $B1$ and $B2$ sites in the figure) and a linear three-atom chain (the $B3$ and $C4$ sites in the figure) along the threefold diagonal axis of the conventional cell. However, the very similar scattering factors of ^{11}B and ^{12}C for both x rays and neutrons rendered the diffraction studies insensitive to the locations of the carbon in the unit cell.[20]

Consequently, less-direct transport measurements such as electrical conductivity, thermoelectric Seebeck coefficients, and Hall constant,[21–23] in addition to other spectroscopic techniques such as infrared,[24] optical Raman,[25] NMR,[26,27] electron energy loss spectroscopy (EELS),[28] and x-ray absorption near-edge structure[29–32] (XANES) have been used to address this puzzle. A variety of compositional models for the three-atom chain have also been proposed, each characterized by different carbon occupancy on the icosahedral sites.[14,33,34] The most recent density functional theory calculations have succeeded in interpreting part of the infrared, Raman, and NMR spectra as favoring CBC for the composition of the three-atom chain.[33]

Here we will utilize core-exciton spectroscopy using both q-dependent x-ray Raman scattering (XRS) (Refs. 35–38) measurements and *ab initio* calculations.[39] Traditionally, core excitation spectra such as XANES and EELS have been widely interpreted using the molecular orbital theory.[40] However, the careful consideration of many-body effects in *ab initio* calculation schemes have made tremendous advances, allowing quantitative comparison with experiments in the near-edge region.[39,41] The fact that these calculations yield not only the absorption coefficient but also the projected density of states (l-DOS) (Ref. 35) for the final state provides an additional spectroscopic tool which can be exploited in XRS, but not in XANES or EELS. Specifically, XRS allows one to simultaneously control the photoelectron energy *and* momentum; this latter degree of freedom, which is absent in XANES and of only limited value in EELS, makes XRS uniquely well suited to study multipole contributions to the transition probability. In our case, the combination of *ab initio* theory and q-dependent XRS convincingly resolves a key part of the site-substitution disorder problem: we find dominant boron occupation at the $B3$ site. This conclusion is further supported by general symmetry considerations, i.e., through a general relationship between site-specific inversion symmetry and parity conservation. This is the first time that XRS has been used to address a site-substitution disorder problem.

In the sections that follow we will present and discuss our evidence for a p-type core exciton from the $B3$ site in B$_4$C. In Sec. II, we review the theory of XRS and highlight the important differences between XRS and traditional x-ray absorption spectroscopies (XAS). In particular, we emphasize that the transition matrix element can no longer be solely treated in the dipole limit but instead the full multipole expansion of the photoelectron wave function must be considered. The experimental results are presented in Sec. III. Their most significant feature is a near-edge peak having monotonically decreasing intensity with increasing q. Site-specific *ab initio* calculations for a wide range of structural models of carbon occupation are presented in Sec. IV and provide two
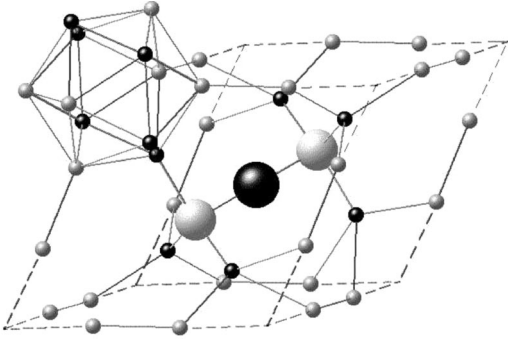
FIG. 1. The unit cell of the B_{12}-CBC structure has four distinct crystallographic sites (Ref. 14). Six $B1$ (small black sphere) 'equatorial' sites and six $B2$ (small white sphere) "polar" sites form an icosahedron. The chain-end sites are labeled $C4$ (large white sphere) while the chain-center is called $B3$ (large black sphere). Sites involved in other models for site substitution on the chains retain the numerical index, i.e., a boron atom at a chain-end site is referred to as $B4$. The sticks are not indications of chemical bonds, but of the nearest-neighbor relationships and the boundary of the unit cell.

major predictions about the near-edge peak. First, that it must be due to dominant boron occupancy of the $B3$ site. Second, that it is a p-type exciton. These hypotheses are critically tested in Sec. V by consideration of the q-dependence of the XRS. The experimentally observed q dependence of the near-edge peak is fundamentally inconsistent with s- or d-wave contributions but is instead in qualitative agreement with the predictions of the *ab initio* calculations and also in reasonable quantitative agreement with a simplified model for a purely p-wave exciton. In addition, we argue that the strongly p-type character is necessarily related to the conserved parity of the final state. In B_4C parity conservation is unique to excitations at the $B3$ site, i.e., the only site with inversion symmetry. In Sec. VI, we report additional simulations which address the spatial extent of the exciton and the importance of the full multiple scattering treatment. Finally, we summarize our conclusions in Sec. VII.

II. THEORY

XRS is a weak inelastic scattering process for hard x rays from the K-shell electrons of low-Z elements. In the single electron picture, the dynamic structure factor $S(\mathbf{q},\omega)$ is expressed as[42,43]

$$S(\mathbf{q},\omega)=\sum_f |\langle f|e^{i\mathbf{q}\cdot\mathbf{r}}|0\rangle|^2 \delta(E_f-E_0-\hbar\omega), \quad (1)$$

with the transferred momentum $\mathbf{q}$ as a free parameter uncorrelated to the transferred energy $\hbar\omega$. In the dipole limit of small $\mathbf{q}$, Equation (1) simplifies to give the same K-edge spectrum as EELS and XAS.[42]

However, XRS has two important features which can result in information complementary to or inaccessible by EELS and XAS. First, the use of hard x rays renders XRS a bulk technique, which not only implies a lack of sensitivity

to surface contamination but also allows potential applications to situations not compatible with the high-vacuum conditions required by EELS and soft-x-ray XAS. Second, it is often possible to measure XRS over a wide enough range of momentum transfer to identify some aspects of the multipole components of the final state.[35–39] In recent years, $\mathbf{q}$-dependent XRS has revealed many-body final state effects both in metals[35,38] and insulators.[36,37]

Following the short-range order theory[44] and the general guidelines of Doniach *et al.*,[43] the angular parts of both the electron wave functions and the transition matrix element are expanded in the spherical harmonics basis as

$$\psi_f(\mathbf{r})=\sum_{l'm'} R^f_{l'm'}(r)Y_{l'm'}(\theta,\varphi)$$

and

$$e^{i\mathbf{q}\cdot\mathbf{r}}=\sum_{l,m} i^l 4\pi j_l(qr)Y_{lm}(\theta_q,\varphi_q)Y^*_{lm}(\theta,\varphi),$$

with $R^f_{l'm'}(r)=\langle Y_{l'm'}|f\rangle$. The initial core state is assumed to be s-type, and the final state is usually a mixture of partial waves because of the ligand-field influence in a solid system. Substitution of these expansions into Eq. (1) separates the angular variables of the transferred momentum $\mathbf{q}$ from its magnitude

$$S(\mathbf{q},\omega)=\sum_f \left|\sum_{lm} s_{flm}(q)Y_{lm}(\theta_q,\varphi_q)\right|^2 \delta(E_f-E_0-\hbar\omega), \quad (2)$$

where

$$s_{flm}(q)=i^l\sqrt{4\pi}\int_0^\infty j_l(qr)R^f_{lm}(r)R_0(r)\cdot r^2 dr$$

is the magnitude of the Y_{lm}-projected momentum space convolution between the initial state $|0\rangle$ and each final state $\langle f|$. $S(\mathbf{q},\omega)$ is now composed of contributions from different multipole (l,m) waves of the final-state wave function, each with a different $\mathbf{q}$-dependence.

To better understand this multipole contribution to $S(\mathbf{q},\omega)$, we will now discuss the projection of the density of states onto different spherical harmonics, which is known as l-DOS. The total electron density $\rho(\mathbf{r},\omega)$ is defined as

$$\rho(\mathbf{r},\omega)=\sum_f \delta(E_f-E_0-\hbar\omega)\psi^*_f(\mathbf{r})\psi_f(\mathbf{r})$$

$$=-\frac{1}{\pi}\text{Im}\,G(\mathbf{r},\mathbf{r},\omega) \quad (3)$$

using a Green's function approach[39] with

$$G(\mathbf{r}',\mathbf{r},\omega)=\langle\mathbf{r}'|G(\omega)|\mathbf{r}\rangle=\frac{\sum_f \psi^*_f(\mathbf{r}')\psi_f(\mathbf{r})}{E_0+\hbar\omega-\mathbf{H}+i\eta^+}.$$

The projected electron density of states (l-DOS) $\rho_l(\omega)$ is consequently defined as

$$\rho_l(\omega) = \sum_m \int_0^{R_{NM}} \rho_{lm}(r,\omega) 4\pi r^2 dr, \qquad (4)$$

where $\rho_{lm}(r,\omega) = -(1/\pi)\text{Im}\langle Y_{lm}|G(\mathbf{r}',\mathbf{r},\omega)|Y_{lm}\rangle|_{r'=r}$, and R_{NM} is a Norman radius.[39] Thus the dynamical structural factor $S(q,\omega)$ is essentially a manifestation of Fermi's golden rule:

$$S(q,\omega) = \frac{1}{4\pi}\int S(\mathbf{q},\omega)d\Omega_{\mathbf{q}} \approx \sum_{lm} \rho_{lm}(\omega)s_{lm}^2(q).$$

For XANES measurements in the dipole limit, only the $l=1$ term dominates. On the other hand, for XRS the different q dependences of different partial waves give a continuous variation of the relative weights on different l-DOS as q increases.

III. EXPERIMENT

All measurements were performed at beamline 20-ID of the PNC-CAT sector located at the Advanced Photon Source in Argonne National Laboratory. Beamline 20-ID (Ref. 45) has been optimized for scanning-energy x-ray spectroscopies and provides a monochromatic beam with ~5 $\times 10^{12}$ photons/sec eV with a bandwidth of 1.3 eV. An 11.4-cm-diameter Si (5, 5, 5) spherically-bent crystal analyzer with a 1-m radius of curvature and 0.010-srad collection angle was used in the Bragg back-scattering geometry; complete experimental details are reported elsewhere.[46]

Micron-size B_4C polycrystalline powder (Alfa Aesar 40504, 99.4%) was packed in a 3-mm-thick disk with two 25-μm Kapton windows and measured in the transmission geometry. The boron K-edge XRS spectra were measured for $q=1.05$, 2.17, 3.83, 5.01, 6.03, 7.09, 8.05, and 9.01 Å^{-1}. The carbon K-shell XRS is observable[46] but too weak and broad to be statistically useful in refining any structural model. The resolution from the elastic peak width varies from a 1.45 to 1.87-eV full width at half maximum (FWHM). The background-free XRS spectra, obtained by subtracting characteristic forms for the Compton background (see Ref. 46 for details), are presented in Fig. 2. The near-edge spectra from that -5 to $+5$-eV range have been numerically broadened to the largest resolution 1.87 eV. The absolute energy shift at the edge is 190.6 ± 0.2 eV. The relative intensities of the different spectra were normalized by integration for energies from 20 to 61 eV past the edge, mimicking the f-sum rule, and naturally introducing a q^2 factor.[46,47]

The near-edge peak present in each spectrum in Fig. 2 is the most significant feature of this system. The same peak has previously been observed in EELS (Ref. 28) and XANES (Refs. 29–31) measurements of B_4C, but is absent from similar measurement of α-rhombohedral boron (α-r-B).[48] This fact is significant because α-r-B consists simply of B_{12} icosahedra without the three-atom chain present in the unit cell of B_4C.[1,9] A site-specific analysis of the contribution to the photoelectron transition spectrum is obviously called for,[31] but has not previously been performed.
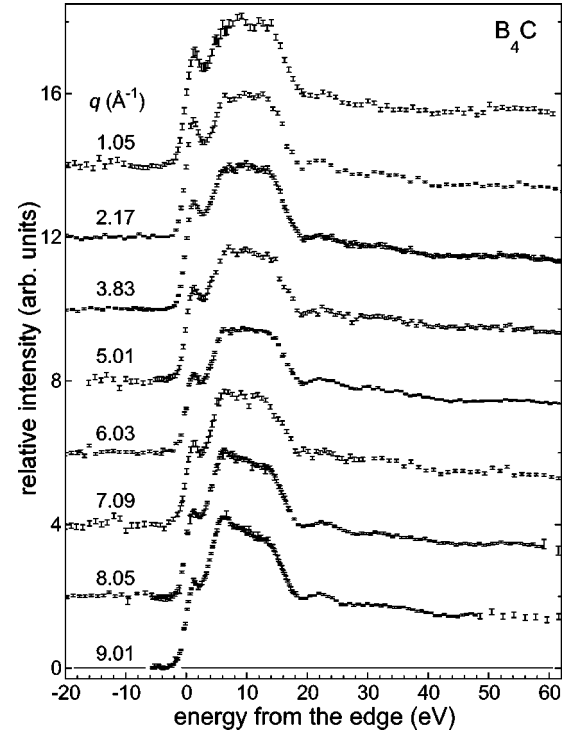

FIG. 2. Boron XRS spectra from B_4C at eight different transferred momenta (from top to bottom): 1.05, 2.17, 3.83, 5.01, 6.03, 7.09, 8.05, and 9.01 Å^{-1}.

IV. SITE-SPECIFIC *AB INITIO* CALCULATIONS

Here, we use FEFF8.28 (Ref. 39) to perform site-specific *ab initio* calculations of the full photoelectron transition probability and projected density of states (l-DOS) for this process. This software has proven reliable in numerous XAS studies.[38,49,50] It uses a real space full multiple-scattering scheme analogous to the Korringa-Kahr-Rostocker Green's function method with a Hedin-Lundqvist self-energy. As listed in Table I, five crystalline structures have been studied. This includes all of the basic models which have been proposed for site occupancy of carbon in B_4C. Note that B_{12}-BBB is not a legitimate structural model since at least one carbon is required in the B_4C unit cell to make it stable; otherwise the pure boron phase would be α-r-B, with an icosahedron on every vertex of the rhombohedral unit-cell, but lacking the three-atom chain. The variation in carbon concentration was also taken into account in simulations, using bare structural data taken from a recent neutron diffraction study of B_4C with different carbon concentrations.[14] The core-hole potential was included in each simulation and is important; we will discuss this in more detail below.

The simulated absolute cross-sections for the boron sites of each of these five structures are plotted in Figs. 3 and 4. One of the major results of this paper is that only the $B3$-site spectra possess a strong near-edge peak, and that this is true for *every* model composition studied. Note that the small peaks at this location in some of the $B1$ and $B2$-site calculations disappear when the effects of instrumental broadening (1.87 eV) are included.

Focusing on the B_{12}-CBC structure, as we show in Fig. 5,

TABLE I. List of crystalline structures used in simulations.

Structure (icosahedron+chain)	Independent crystalline sites	Lattice parameters used from Ref. 14 for carbon concentration of:
B_{12}-BBC	$B1a$, $B1b$, $B2a$, $B2b$, $B3$, $B4$, $C4$	10%
B_{12}-CBC	$B1$, $B2$, $B3$, $C4$	13%
B_{12}-CCC	$B1$, $B2$, $C3$, $C4$	20%
B_9C_3-BBB (carbon on site 1's)	$C1a$, $B1b$, $B2a$, $B2b$, $B3$, $B4a$, $B4b$	20%
B_9C_3-BBB (carbon on site 2's)	$B1a$, $B1b$, $C2a$, $B2b$, $B3$, $B4a$, $B4b$	20%

stoichiometric addition (solid line) of these $B1$, $B2$, and $B3$ calculations after Gaussian broadening to the instrumental resolution of 1.87-eV FWHM results in reasonably good agreement with our experimental data (filled circles with error bars) at a relatively low $q = 3.83$ Å^{-1}. The dashed line in Fig. 5 corresponds to the addition of only the $B1$ and $B2$ sites. Hence, these calculations strongly suggest that the near-edge peak in the XRS spectrum is due to dominant boron occupation at the $B3$ site. Note, however, that the results are otherwise insensitive to the details of site-substitution.

The discussion above was entirely within the context of the dipole limit. However, one of the unique advantages of XRS in comparison to more traditional XANES measurements is the ability to control both the energy *and* momentum of the photoelectron, allowing the investigation of mul-

tipole effects. Hence, prior to discussing the experimentally-observed q-dependence of the XRS in Sec. V, we present calculations of the l-DOS for the $B3$ site (Fig. 6).

Comparing calculations with and without the core-hole effect (solid and fine-dashed lines, respectively), the near-edge peak is identified as an exciton, and the core-hole effect is significant for the first 35 eV of the edge, as is typical for XANES region.[39,51] In addition, the calculations demonstrate that the nature of this exciton is strongly p-type, with s- and d-type components (Fig. 6) at least 100 times smaller. This peak has previously been explained as a π^* resonance, characteristic of the chemical bonding in the CBC chain.[30,31] As we will explain in Sec. VI, however, the range of the exciton and especially the absence of dominant scattering paths
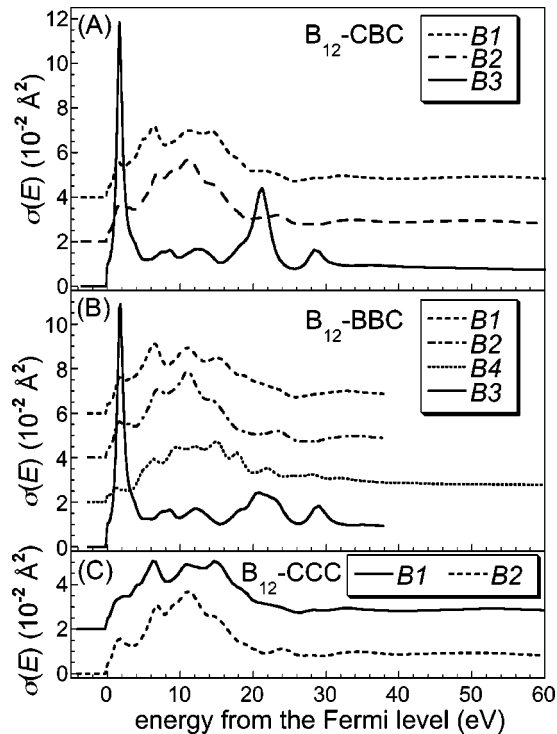

FIG. 3. FEFF simulations of absorption coefficients from three different crystalline structures of boron carbide: (A) B_{12}-BBC, (B) B_{12}-CBC, and (C) B_{12}-CCC. See Fig. 1 for an explanation of the notation for crystallographic sites.
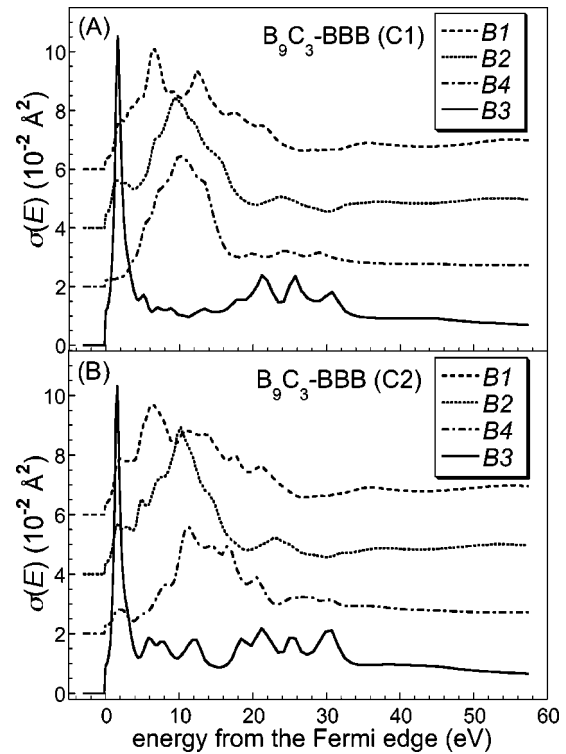

FIG. 4. FEFF simulations of absorption coefficients from two additional crystalline structures of boron carbide: (A) B_9C_3-BBB with all carbons on $C1$ sites forming triangles. (B) B_9C_3-BBB with all carbons on $C2$ sites forming triangles. See Fig. 1 for an explanation of the notation for crystallographic sites.
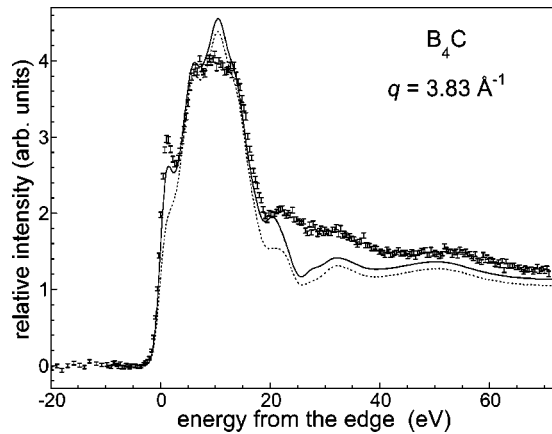
FIG. 5. Comparison of experimental XRS (solid dots with error bars) and simulations for B_{12}-CBC including all atoms (solid line) and only icosahedral sites (dashed line).

along the CBC chain are inconsistent with the molecular orbital interpretation.

In summary, our dipole-limit calculations suggest that the pre-edge peak observed in our low-q XRS data and in the prior EELS (Ref. 28) and XANES (Refs. 29–32) studies is due to dominant boron occupation of the $B3$ site. This is consistent with the most recent studies on NMR and infrared results.[33] Also, calculations of the l-DOS specifically conclude that this feature is a p-type exciton; we will investigate this prediction below.

V. THE q-DEPENDENCE OF THE EXCITON AND INVERSION SYMMETRY

Given the above prediction of a p-type exciton and the prior success of XRS in unambiguously identifying different single-typed excitons in Li,[35] LiF,[36] and h-BN,[37] one is led to investigate the q-dependence of the boron XRS from B_4C. In order to approximately separate the proposed exciton feature from the primary $B1$ and $B2$ contributions to XRS spectra,
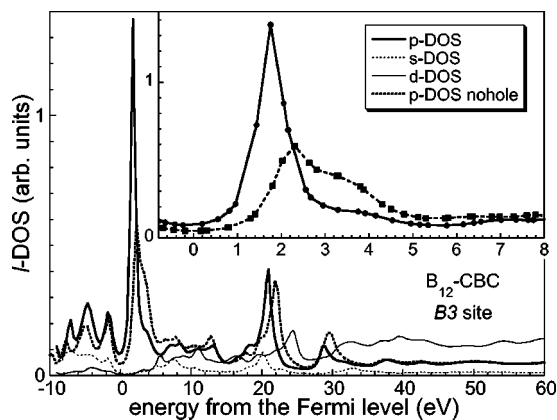

FIG. 6. Projected density of states (l-DOS) at the $B3$ site of the B_{12}-CBC structure. The two p-DOS calculated with and without the core-hole effect indicate the excitonic nature of the near-edge peak (see inset). The exciton is strongly p type, with s- and d-DOS suppressed by a factor of 10^2.
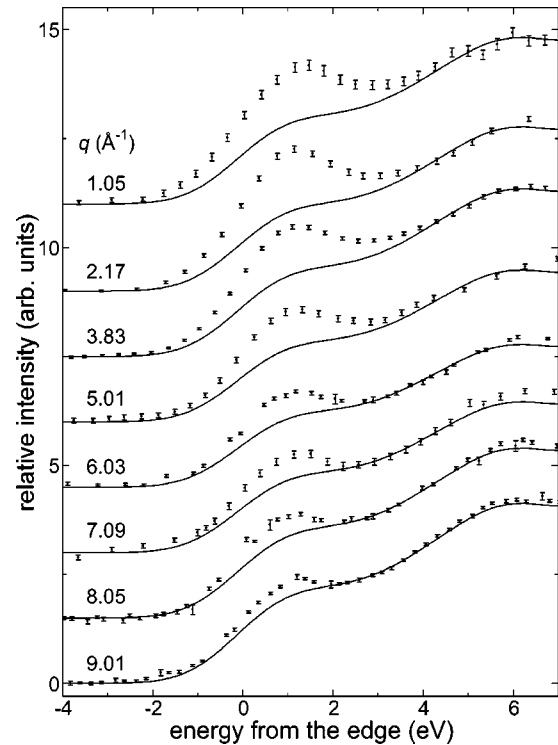

FIG. 7. Enlarged view of the near-edge region for the boron XRS spectra for B_4C (points), compare with Fig. 2. The solid lines are the estimated $B1+B2$ background for the B_{12}-CBC structure, compare with Fig. 5. Note the steady decrease in the intensity of the pre-edge feature with increasing q.

we first scale the $B1+B2$ contribution to best fit the main edge intensity and shape at different q's, as shown in Fig. 7. Clearly, there is a monotonic decrease in the intensity of the pre-edge peak with increasing q. In Fig. 8 we show the areas underneath the near-edge peaks are integrated from -4 to 5 eV after subtraction of the estimated $B1+B2$ contribution to the spectrum; the error bars representing the combination of statistical uncertainties and 1% of the subtracted intensity due to the statistical uncertainty of the fitting scaling factors.
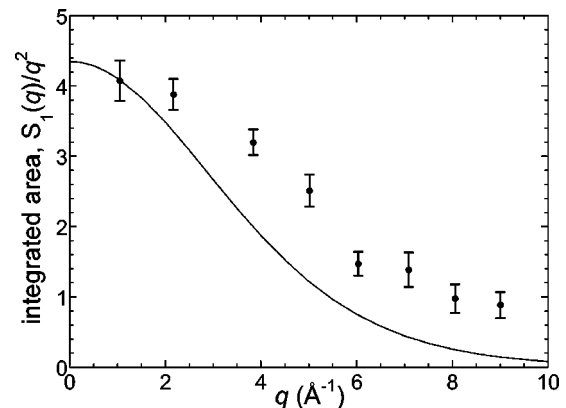

FIG. 8. The q-dependence of the p-type exciton. (solid dots with error bars): integrated exciton weight from experimental XRS data. (solid curve): theoretical calculation of $S_{1s-2p}(q)/q^2$ from a 1s to a hydrogen-like $2p$ orbital in a boron atom. [Eq. (5)].

The dominant source of systematic error (which may be substantial) in this analysis is of course from the reliability of the simulated $B1+B2$ background. There are two possible forms of such an error: the shape of the $B1+B2$ background in the near-edge region may be incorrect at the fine level of Fig. 7, or there may be a strong energy-dependence of the q dependence of the background either in the near-edge region of Fig. 7 or in the extended region (which is used for overall spectrum normalization). The first factor is alleviated by the reasonable agreement between our calculated $B1+B2$ background and the core excitation spectrum of α-r-B,[48] which consists entirely of boron icosahedra. As for the second factor, it is important to note that the $B1$ and $B2$ sites are of relatively low-symmetry, and correspondingly the l-DOS calculations at these sites[46] show a strong admixture of different partial-waves at all energies, with essentially the same energy dependence for s-, p-, and d-DOS for the first 20 eV above the Fermi level. We believe, then, that a conservative estimate of the systematic error in Fig. 8 is 20%. Such an error is insufficient to remove the strong decrease in intensity of the pre-edge feature with increasing q.

This monotonically decreasing $S(q)/q^2$ for the exciton shown in Figs. 7 and 8 is typical of a p-type exciton.[37,43] Note that $S(q)$ of the observed s-type exciton in LiF (Ref. 36) and the predicted d-type exciton[43] show the opposite behavior: $S(q)/q^2 = 0$ at $q=0$, and a steady increase with increasing q.

The complex structure of B_4C does not presently allow a q-dependent *ab initio* calculation of $s_{lm}(q)$. Here we have to rely on a crude model of transition between an $1s$ and a hydrogen-like $2p$ final state for a semi-quantitative explanation of the observed q-dependence of the exciton shown in Fig. 8. The dynamical structure factor $S(q,\omega)$ can be expressed as a sum of partial wave contributions, after averaging over the **q** direction for a powder sample, i.e.,

$$S_{1s-2p}(q) \propto \left| \int dr \cdot r^2 R_{2p}(r) j_1(qr) R_{1s}(r) \right|^2 \propto q^2/(k^2+q^2)^6. \quad (5)$$

Here $k = (Z+Z'/2\varepsilon)/a_0$; $Z' = Z+1$ is the equivalent atomic number for the core-hole potential; and $\varepsilon = 7$ is a reasonable value for the static dielectric constant of the material. $S_{1s-2p}(q)/q^2$ is plotted in Fig. 8 (solid curve) with a single free parameter to scale the overall amplitude, but not, e.g., the parameter $k = 10.3$ Å^{-1}, which determines the half width of the curve and is set purely by atomic physics: boron's atomic number Z and the Bohr radius a_0. The agreement on the overall q dependence between experiment and this simple theory is additional evidence in favor of a p-type exciton.

Further support for this conclusion comes from general symmetry considerations. Single-typed excitons have to be associated with a strong local symmetry.[37] Here the $B3$ site is unique in the B_4C unit cell as being the only site with inversion symmetry. The presence of inversion symmetry requires both the initial and final states to be eigenstates of parity, and the fact that the lowest empty $2p$ state in boron has different parity than the s and d states leads naturally to
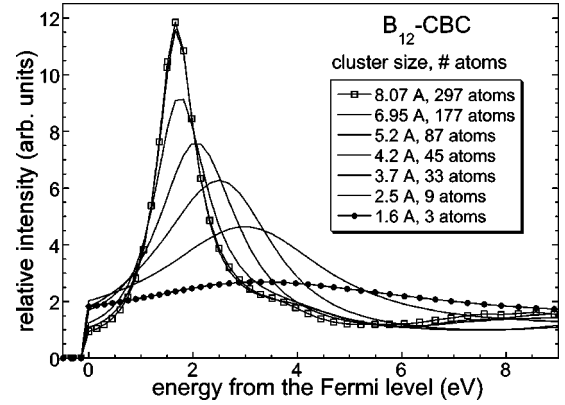

FIG. 9. Convergence of simulations of the exciton with increasing cluster size. Note that the simulations essentially overlap for radii of 6.95 and 8.07 Å.

a physical explanation for the observed p-type character. In future studies, we propose that the occurrence of single-typed excitons can be used as a spectroscopic indication of strong local symmetries. For example, elsewhere we report our measurements of a purely p-type exciton in hexagonal BN.[37,46] This strongly anisotropic system has only reflection (rather than inversion) symmetry, a fact with significant consequences for the angular characteristics of the excitation.[37]

VI. SPATIAL PROPERTIES OF THE EXCITON AND THE IMPORTANCE OF FMS

So far we have deduced the existence of a p-type exciton from both experimental and theoretical approaches. However, further knowledge about this excitation is still available. In this section, we will perform additional simulations to explore the spatial properties of this exciton state, and to investigate whether a small number of photoelectron scattering paths might dominate or if instead the full multiple scattering (FMS) approach used in this study is indeed critical.

First, note that the dynamic structure factor $S(\mathbf{q},\omega)$ is indeed a convolution of initial and final electron states in momentum space

$$S(\mathbf{q},\omega) = \sum_f |\langle f|e^{i\mathbf{qr}}|0\rangle|^2 \delta(\Delta E - \hbar\omega)$$

$$= \sum_f \left| \int \psi_f(\mathbf{p}-\mathbf{q})\psi_0(\mathbf{p})d\mathbf{p} \right|^2 \delta(\Delta E - \hbar\omega). \quad (6)$$

Thus the q-dependence is actually a measure of the momentum distribution of the photoelectron in the final exciton state. On the other hand, the spatial extent of the photoelectron in the exciton state can also be determined by studying the convergence of the FMS calculation with an increasing cluster size,[50] as shown in Fig. 9. Simulations of the exciton converge with a 200 atoms cluster of a radius about 7 Å. This is considerably beyond the unit-cell-sized cluster of 2.95-Å radius, and is consistent with the extent of a $2p$ state in a statically screened core-hole field as calculated in Eq. (5),

i.e., radial distribution of the electron density maximizes at 2.6 Å, and 99% of the total electron density are within the 7-Å radius.

Second, we do indeed find that the FMS scheme used here is critical for near-edge simulations of the B_4C system. For comparison, the traditional multiple-scattering (MS) path expansion was carried out for up to eight scattering legs and a total path length of 12.4 Å. Similar parameters were used for approximations of FMS by MS, and allowed discussions of dominant photoelectron scattering paths in model extended x-ray absorption fine structure (EXAFS) studies of molecular O_2 (Ref. 52) and Cu systems.[53] However, the analogous calculations here failed to converge for B_4C system and no dominant scattering paths were found. There are two explanations for this observation. First, the relatively low local-symmetry in B_4C results in a low degeneracy for photoelectron scattering paths. Second, while the occurrence of dominant scattering paths in the extended region of XAFS is well understood,[54] this phenomenon may not extend into the near-edge region. In particular, the low photoelectron energy results in essentially isotropic (s-wave) scattering, unlike in the extended XAFS region where the higher photoelectron energy leads to strongly anisotropic scattering which, in turn, can give so-called focusing effects and strong back scattering among other mechanisms leading to a finite number of scattering paths with dominant weight in the overall cross-section.

On the other hand, recent developments using the Lanczos algorithms[55] allow one to directly test the order of MS needed for convergence by iteratively increasing the number of scattering legs in the calculation. In Fig. 10 we show the results of such a calculation for the $B3$ site. The solid curve and left axis refer to the calculated absolute cross section, while the right axis and crosses ($+$) provide the number of scattering legs needed for convergence at the specified energy from the Fermi edge. Note that over 100 scattering legs are needed in the near-edge region, again emphasizing the importance of the FMS approach for the near-edge region.

Taken *en masse*, these additional calculations provide further evidence for an extended exciton of the $B3$ site. Both the range of the exciton and the absence of dominant scattering paths (especially along the $C4$-$B3$-$C4$ chain) are also contrary to the prior explanation of the pre-edge feature as a π^* local resonance from the $B3$-$C4$ pair.[30,31]
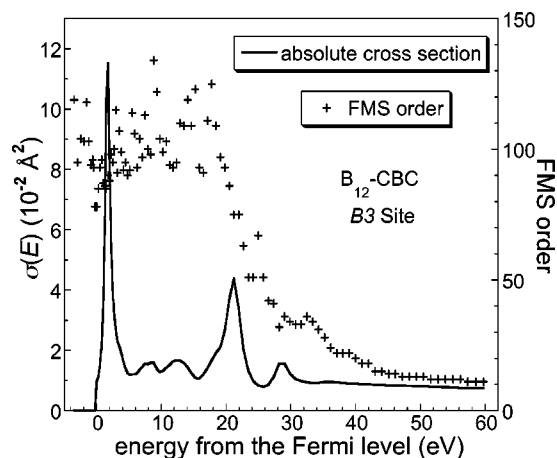

FIG. 10. (Solid line and left axis): The calculated absorption coefficient for the $B3$ site in B_{12}-CBC. (Crosses and right axis): The number of scattering legs required for convergence of a multiple scattering calculation, as determined by the iterative Lanczos algorithm.

VII. CONCLUSION

In conclusion, using q-dependent non-resonant x-ray Raman scattering (XRS) and *ab initio* calculations, we find conclusive evidence for dominant boron occupation of the chain-center $B3$ site in B_4C and an associated delocalized p-type exciton. To our knowledge this is the first time that XRS has been used to address site-substitutional disorder. The methodology of this study may prove useful in other cases where site-substitutional disorder occurs for sites with very different symmetries. We also propose that the occurrence of single-typed excitons can be used as a spectroscopic indication of strong local symmetries in future studies.[37,46]

*Corresponding author. Email address: seidler@phys.washington.edu

[1] D. Emin, Phys. Today **40**(1), 55 (1987).

[2] J. Haines, J. M. Léger, and G. Bocquillon, Annu. Rev. Mater. Sci. **31**, 1 (2001).

[3] R. J. Nelmes, J. S. Loveday, R. M. Wilson, W. G. Marshall, J. M. Besson, S. Klotz, G. Hamel, T. L. Aselage, and S. Hull, Phys. Rev. Lett. **74**, 2268 (1995).

[4] M. Somayazulu, J. Akella, S. T. Weir, D. Häusermann, G. Shen, Advance Photon Source Activity Reports 2000, Argonne National Laboratory (ANL-01/03), December (2001).

[5] O. A. Golikova, Phys. Status Solidi A **101**, 277 (1987); **51**, 11 (1979).

[6] W. N. Lipscomb, *Boron Hydrides* (Benjamin, New York, 1963).

[7] H. C. Longuet-Higgins and M. de V. Roberts, Proc. R. Soc. London, Ser. A **230**, 110 (1955).

[8] M. Fujimori, T. Nakata, T. Nakayama, E. Nishibori, K. Kimura, M. Takata, and M. Sakata, Phys. Rev. Lett. **82**, 4452 (1999).

[9] J. Donohue, *The Structures of the Elements* (Wiley, New York, 1974).

[10] M. Vlasse, R. Naslain, J. S. Kasper, and K. Ploog, J. Solid State Chem. **28**, 289 (1979).

[11] H. Hubert, B. Devouard, L. A. J. Garvie, M. O'Keeffe, P. R. Buseck, W. T. Petuskey, and P. F. McMillan, Nature (London) **391**, 376 (1998).

[12] C. L. Perkins, M. Trenary, and T. Tanaka, Phys. Rev. B **58**, 9980 (1998); Phys. Rev. Lett. **77**, 4772 (1996).

[13] M. Bouchacourt and F. Thevenot, J. Less-Common Met. **82**, 219 (1981).

[14] G. H. Kwei and B. Morosin, J. Phys. Chem. **100**, 8031 (1996); B. Morosin, G. H. Kwei, A. C. Larson, T. L. Aselage, and D. Emin, J. Alloys Compd. **226**, 121 (1995).

[15] B. Morosin, A. W. Mullendore, D. Emin, and G. A. Slack, in *Boron-Rich Solids*, edited by D. Emin, AIP Conf. Proc. No. 140 (AIP, New York, 1986), p. 70.

[16] A. Kirfel, A. Gupta, and G. Will, Acta Crystallogr., Sect. B: Struct. Crystallogr. Cryst. Chem. **35**, 1052 (1980).

[17] H. L. Yakel, Acta Crystallogr., Sect. B: Struct. Crystallogr. Cryst. Chem. **31**, 1797 (1975).

[18] A. C. Larson and D. T. Cromer, Acta Crystallogr., Sect. A: Cryst. Phys., Diffr., Theor. Gen. Crystallogr. **28**, S53 (1972).

[19] A. Lipp, Ber. Dtsch. Keram. Ges. **43**, 60 H1 (1966).

[20] ^{10}B, 20% natural abundance, is a strong neutron absorber, and the coherent neutron scattering lengths for ^{11}B, ^{12}C, and ^{13}C are 6.65, 6.6535, and 6.19 fm respectively.

[21] T. L. Aselage, D. Emin, and S. S. McCready, Phys. Rev. B **64**, 054302 (2001).

[22] T. L. Aselage, D. Emin, S. S. McCready, and R. V. Duncan, Phys. Rev. Lett. **81**, 2316 (1998).

[23] C. Wood and D. Emin, Phys. Rev. B **29**, 4582 (1984).

[24] U. Kuhlmann, H. Werheit, and K. A. Schwetz, J. Alloys Compd. **189**, 249 (1992).

[25] D. R. Tallant, T. L. Aselage, A. N. Campbell, and D. Emin, Phys. Rev. B **40**, 5649 (1989).

[26] M. N. Alexander, in *Boron-Rich Solids* (Ref. 15), p. 168.

[27] T. M. Duncan, in *Boron-Rich Solids* (Ref. 15), p. 177; J. Am. Chem. Soc. **106**, 2270 (1984).

[28] P. Favia, T. Stoto, M. Carrard, P.-A. Stadelmann, and L. Zuppiroli, Microsc. Microanal. Microstruct. **7**, 225 (1996).

[29] J. J. Jia, J. H. Underwood, E. M. Gullikson, T. A. Callcott, and R. C. C. Perera, J. Electron Spectrosc. Relat. Phenom. **80**, 509 (1996).

[30] D. Li, G. M. Bancroft, and M. E. Fleet, J. Electron Spectrosc. Relat. Phenom. **79**, 71 (1996).

[31] I. Jiménez, L. J. Terminello, F. J. Himpsel, M. Grush, and T. A. Callcott, J. Electron Spectrosc. Relat. Phenom. **101−103**, 611 (1999).

[32] I. Jiménez, D. G. J. Sutherland, T. van Buuren, J. A. Carlisle, L. J. Terminello, and F. J. Himpsel, Phys. Rev. B **57**, 13167 (1998).

[33] F. Mauri, N. Vast, and C. J. Pickard, Phys. Rev. Lett. **87**, 085506 (2001); R. Lazzari, N. Vast, J. M. Besson, S. Baroni, and A. Dal Corso, *ibid.* **83**, 3230 (1999).

[34] D. Emin, Phys. Rev. B **38**, 6041 (1988).

[35] M. H. Krisch, F. Sette, C. Masciovecchio, and R. Verbeni, Phys. Rev. Lett. **78**, 2843 (1997).

[36] K. Hämäläinen, S. Galambosi, J. A. Soininen, E. L. Shirley, and A. Shukla, Phys. Rev. B **65**, 155111 (2002).

[37] Yejun Feng, J. A. Soininen, A. L. Ankudinov, G. T. Seidler, J. O. Cross, A. T. Macrander, J. J. Rehr, and E. L. Shirley (unpublished).

[38] C. Sternemann, M. Volmer, J. A. Soininen, H. Nagasawa, M. Paulus, H. Enkisch, G. Schmidt, M. Tolan, and W. Shülke, Phys. Rev. B **68**, 035111 (2003).

[39] A. L. Ankudinov, B. Ravel, J. J. Rehr, and S. D. Conradson, Phys. Rev. B **58**, 7565 (1998).

[40] J. Stöhr, *NEXAFS Spectroscopy* (Springer-Verlag, Berlin, 1992).

[41] E. L. Shirley, J. Electron Spectrosc. Relat. Phenom. **110−111**, 305 (2001).

[42] Y. Mizuno and Y. Ohmura, J. Phys. Soc. Jpn. **22**, 445 (1967).

[43] S. Doniach, P. M. Platzman, and J. T. Yue, Phys. Rev. B **4**, 3345 (1971).

[44] W. L. Schaich, Phys. Rev. B **8**, 4028 (1973).

[45] S. Heald, E. Stern, D. Brewe, R. Gordon, D. Crozier, D. Jiang, and J. Cross, J. Synchrotron Radiat. **8**, 342 (2001).

[46] Yejun Feng, Ph.D. dissertation, University of Washington, 2003.

[47] D. Pines, P. Nozières, *The Theory of Quantum Liquids* (Benjamin, New York, 1966), Vol. 1.

[48] M. Terauchi, Y. Kawamata, M. Tanaka, M. Takeda, and K. Kimura, J. Solid State Chem. **133**, 156 (1997).

[49] J. J. Rehr and R. C. Albers, Rev. Mod. Phys. **72**, 621 (2000).

[50] F. Farges, G. E. Brown, and J. J. Rehr, Phys. Rev. B **56**, 1809 (1997).

[51] L. A. Grunes, Phys. Rev. B **27**, 2111 (1983).

[52] J. J. Rehr, R. C. Albers, and S. I. Zabinsky, Phys. Rev. Lett. **69**, 3397 (1992).

[53] S. I. Zabinsky, J. J. Rehr, A. Ankudinov, R. C. Albers, and M. J. Eller, Phys. Rev. B **52**, 2995 (1995).

[54] G. Bunker and E. A. Stern, Phys. Rev. Lett. **52**, 1990 (1984).

[55] A. L. Ankudinov, C. E. Bouldin, J. J. Rehr, J. Sims, and H. Hung, Phys. Rev. B **65**, 104107 (2002).